Nationaal Lucht- en Ruimtevaartlaboratorium
National Aerospace Laboratory NLR

NLR-TP-2002-460

The boundary conforming discontinuous Galerkin finite element approach for rotorcraft simulations

O.J. Boelens, H. van der Ven, B. Oskam and A.A. Hassan

NLR-TP-2002-460

The boundary conforming discontinuous Galerkin finite element approach for rotorcraft simulations

O.J. Boelens, H. van der Ven, B. Oskam and A.A. Hassan*

* The Boeing Company (Mesa)

This report is based on an article first submitted to the Journal of Aircraft on 28 September 2001, and in a second Revised Version on 2 May 2002.

Customer:	National Aerospace Laboratory NLR
Working Plan number:	1.1.H.2h
Owner:	National Aerospace Laboratory NLR
Division:	Fluid Dynamics
Distribution:	Unlimited
Classification title:	Unclassified
	July 2002

Summary

A numerical method has been developed for predicting the complex vortex-wake for a helicopter rotor in hover and in forward flight. The method is based on the solution of the three-dimensional, compressible Euler equations expressed in an Arbitrary Lagrangian Eulerian (ALE) reference frame. A second-order accurate discontinuous Galerkin (DG) finite-element method is used to discretize the governing equations on a hexahedral mesh. Unstructured, local mesh refinement is performed to enable prediction of the structure of the vortex-wake. The capabilities of this CFD method are demonstrated by simulations of the flow around the Caradonna-Tung helicopter rotor in hover and simulations of the flow around the Operational Loads Survey helicopter rotor in forward flight. Accuracy of the method is assessed through comparison with wind tunnel data, if available. Special attention is given to a rotor trimming procedure developed at NLR, and the grid adaptation algorithm.

Contents

1 Introduction **9**
1.1 Rotor flow prediction methods 9
1.2 State-of-the-art flow solvers for helicopter rotors in forward flight 9
1.3 Outline of report 10

2 CFD algorithm **10**
2.1 Discontinuous Galerkin method 10
2.2 Unique features 11

3 Rotor trimming **12**

4 Grid adaptation **13**

5 Rotorcraft simulations **15**
5.1 Caradonna-Tung helicopter rotor in hover 15
5.2 Operational Loads Survey helicopter rotor simulations 16

6 Summary **19**

7 Conclusions **20**

(29 pages in total)

List of figures

Figure 1: Surface pressure ($-C_p$) distribution at the radial stations r/R=0.68 (a), 0.89 (b) and 0.96 (c) for the Caradonna-Tung helicopter rotor in hover (collective pitch angle: 12 degrees, tip Mach umber: 0.61, Reynolds number: $2.7 \cdot 10^6$). 26

Figure 2: Sectional thrust for the Caradonna-Tung helicopter rotor in hover for the 'medium grid' with adaptation (135,280 elements), the 'fine grid' (726,784 elements) and the experiment[8] (collective pitch angle: 12 degrees, tip Mach number: 0.61). 26

Figure 3: Vorticity contours at the 140 degree azimuth location behind the blade for the Caradonna-Tung helicopter rotor in hover on the 'medium grid' with adaptation (a) (135,280 elements) and on the 'fine grid' (b) (726,784 elements) (collective pitch angle: 12 degrees, tip Mach number: 0.61). 26

Figure 4: The adapted Caradonna-Tung grid (135,280 elements). 27

Figure 5: Iso-contour of the vorticity for the Caradonna-Tung helicopter rotor in hover on the 'fine grid' (726,784 elements) (collective pitch: 12°, M_{tip}=0.61). 27

Figure 6: Predicted and experimental vortex trajectory of the Caradonna-Tung rotor in hover on the 'medium grid' with adaptation (135,280 elements and on the 'fine grid' (726,784 elements) (collective pitch angle: 12 degrees, tip Mach number: 0.61). 27

Figure 7: Differential pressure $-\Delta C_p M^2$ at the three percent chordwise station at r/R=0.975 for Schedule 1, Schedule 2 and the experiment. 28

Figure 8: Differential pressure $-\Delta C_p M^2$ at the three percent chordwise station at r/R=0.975 for the Schedule 2, Strawn[26] and the experiment. 28

Figure 9: Differential pressure $-\Delta C_p M^2$ at the three percent chordwise station at the radial stations r/R=0.75 (a), 0.80 (b), 0.85 (c), 0.91 (d) and 0.975 (e) for the Operational Loads Survey helicopter rotor in forward flight. 29

Figure 10: The sectional lift (a), the derivative of the sectional lift with respect to ψ (b), the differential pressure $-\Delta C_p M^2$ at the three percent chordwise station (c) and the derivative of the differential pressure $-\Delta C_p M^2$ at the three percent chordwise station with respect to ψ(d) for Schedule 2. 29

List of tables

Table 1: Pitch and flap angles used in the simulation of the Operational Loads Survey helicopter rotor in forward flight. 24

Table 2: Force and moment data from the simulation of the Operational Loads Survey helicopter rotor in forward flight. 24

Table 3: Qualitative comparison and computing times of existing rotor codes for forward flight simulations. NWT: Numerical Wind Tunnel (parallel vector machine with 1.7 Gflop/s peak per processor), Cray J916: parallel vector machine with 0.5 Gflop/s peak per processor, Cray C-90 24

List of symbols

C_{Mx}	= moment around x-axis
C_{My}	= moment around y-axis
C_p	= surface pressure coefficient
C_T	= thrust coefficient
M	= local Mach number
M_{tip}	= tip Mach number
r	= radial distance along rotor blade
R	= rotor tip radius
x, y, z	= Cartesian coordinates
α_{TPP}	= tip-path plane angle
β_0	= collective flap angle
β_{1c}	= cosine-dependent flap angle
β_{1s}	= sine-dependent flap angle
$-\Delta C_p M^2$	= differential pressure
μ	= advance ratio
θ	= pitch angle
θ_0	= collective pitch angle
θ_{1c}	= cosine-dependent pitch angle
θ_{1s}	= sine-dependent pitch angle
ω	= vorticity
ψ	= azimuth angle

This page is intentionally left blank.

1 Introduction

It is well known that the prediction of the aerodynamic performance of a helicopter in hover or forward flight is dependent on one's ability to accurately predict its complex vortex-wake. To assess the impact of improved airfoil designs, novel blade twist and blade planform on rotor performance, it is essential to consider a tool that can accurately predict the rotor wake system. In the following sections, the advantages and limitations of the available rotor flow prediction methods are summarized, with special attention to wake predictions.

1.1 Rotor flow prediction methods

The presently available solution techniques for predicting the unsteady aerodynamic response of helicopter rotors can be classified in two categories:

(i) vortex based methods, with a rigidly prescribed wake geometry or with a free wake geometry, and

(ii) Euler/Navier-Stokes methods.

Vortex based methods have more severe limitations than the more comprehensive Euler/Navier-Stokes methods. The deficiencies of vortex based methods are related to the additional unknown parameters (e.g., core size parameters), which have a direct influence on the position and/or motion of the vortex.

In recent years, more comprehensive models that are based on the solution of the Euler and the Navier-Stokes equations[3-6,13-17,19-22,24-27,32-34] were developed. The prime objective was to develop solution methods that had minimum reliance on user input while providing the necessary accuracy. In principle, though these formulations are sufficient for capturing the details of the vortical flow field, excessive numerical diffusion, especially in regions far from the blade, limit their application. To minimize numerical diffusion, researchers embarked on adopting one, or more, strategies. Namely, the use of higher-order numerical schemes[17], the use of overset (or Chimera) grid systems to resolve the details of the wake away from the blade[17,27], and the use of adaptive gridding schemes that are natural for unstructured grid flow solvers[3,4,13,14]. Among these three strategies, wake capturing through adaptation of an unstructured grid proved to be the most promising - typically, not requiring excessively large grids as with structured grid flow solvers.

1.2 State-of-the-art flow solvers for helicopter rotors in forward flight

In Tab. 3 an overview is given of the present state-of-the-art flow solvers for the simulation of helicopter rotors in forward flight. The discontinuous Galerkin finite element flow solver discussed in this report is the only flow solver based on the boundary conforming ALE approach. The other codes apply the Chimera or overset approach where sets of partially overlapping grids are used to cover the computational domain. At the grid overlaps flow

interpolation is required, resulting not only in loss of the conservative property, but also increasing the computational costs significantly. Loss of the conservative property is a major concern for the accuracy of the flow solver, and may result in dissipation of vorticity. Ochi[20] and Pahlke[22] report that on parallel vector machines 20 % of the computing time is spent in the flow data exchange between the different grids. Moreover, the use of overlapping grids involves a large amount of communication, which reduces the scalability of the Chimera or overset approach. Correlating the accuracy of the methods and the required flop count shows that the simulation of a rotor in forward flight is a petaflop problem for state-of-the-art algorithms. Hence acceptable turn-around times can only be accomplished on massively parallel computers or by applying newly developed, more efficient algorithms.

1.3 Outline of report

In this report the unique features and the accuracy of a new unstructured flow solver for capturing the wake of helicopter rotors are demonstrated.

First, the features of the discontinuous Galerkin (DG) finite element method are outlined. Next, the rotor trimming procedure for helicopter rotors in forward flight as employed at NLR will be presented. Also a section will be dedicated to the grid adaptation strategy used in the described simulations. Following these discussions, the simulation capabilities of the present CFD method for rotorcraft flows are demonstrated using the results of simulations of

- the flow around the Caradonna-Tung helicopter rotor in hover, and
- the flow around the Operational Loads Survey helicopter rotor in forward flight.

The results of these simulations will be compared with experimental data, if available. A summary and conclusions complete the report.

2 CFD algorithm

2.1 Discontinuous Galerkin method

The flow solver is based on a discontinuous Galerkin finite element discretization of the unsteady compressible Euler equations[10,11,28].

Discontinuous Galerkin finite element methods use a discontinuous function space to approximate the exact solution of the Euler equations. The discontinuous Galerkin finite element method is a mixture of a finite element and an upwind finite volume method. The flow domain is discretized into a large number of hexahedral elements. The polynomial expansions of the flow field variables are purely element-based and there will be, in general, a discontinuity in the flow field variables across element faces, with as magnitude the truncation error in the polynomial representation. This discontinuity at element faces is interpreted as a one-dimensional Riemann problem, which is used to obtain a unique definition of element face

fluxes. The use of a Riemann problem in the flux calculations has a significant effect in that it introduces upwinding into the finite element discretization. A short introduction to these DG methods is provided in the lecture notes of a NATO special course on *Higher Order Discretization Methods in CFD*[10].

2.2 Unique features

A unique feature of the present second-order accurate discontinuous Galerkin finite element method is that equations are solved not only for the traditional five mean flow field variables, but also for their spatial gradients. This results in a very compact scheme, because it is not necessary to reconstruct the flow field gradients, necessary to achieve second-order accuracy, using data in neighboring elements. The present finite element method has shock capturing capabilities and is easy to parallelize since there is limited communication between neighboring elements. The local character of the present finite element method is also beneficial for grid adaptation, which is carried out using anisotropic grid refinement.

The DG finite element method has an inherent ability to handle adaptivity strategies since the refining and de-refining of the grid is done without taking into account the continuity restrictions of conventional CFD methods[12,28-30]. At this point it should be remarked that in the present research *h*-refinement is utilized to construct an isotropic grid from an anisotropic, initial grid. The anisotropy (elements having large aspect ratios) of the initial grid is often a concomitant feature of efficient, boundary conforming structured grids.

Dynamic motions of multiple moving bodies are simulated using a single, deforming, boundary conforming mesh. The Euler equations on such a mesh are discretized simultaneously in space and time, leading to an Arbitrary Lagrangian Eulerian (ALE) formulation, which incorporates the grid velocities in the flux formulation. Consequently, a conservative scheme that has the same accuracy as the standard DG method for a rigid mesh is obtained. In addition to the governing equations used to evaluate the flow field gradients in space, equations are also solved for the flow field temporal gradients. A clear advantage of this solution method is manifest in its ability to use non-uniform time steps without sacrificing temporal accuracy. For unsteady rotor computations (e.g., for a rotor in forward flight), this feature can be used to reduce the overall required CPU time (number of azimuthal steps) for the computation of a rotor revolution. This efficiency, of course, is achieved at the expense of increased memory requirement due to the additional equations being solved for the temporal derivatives of the flow field variables. The equations are solved implicitly by introducing a pseudo-time and marching the solution to a steady state using a standard FAS multigrid scheme. In this way, the ALE method using a single deforming mesh retains the excellent parallelizability properties of the explicit DG method on rigid meshes.

3 Rotor trimming

A fair comparison between experimental data and numerical simulations can only be obtained if for both cases the helicopter rotor is operating at the same thrust coefficient. Since the experimental thrust coefficient is fixed, the thrust coefficient obtained during the simulations has to be adjusted in such a way that it matches the experimental one. This adjustment or trimming procedure means that the pitch, flap and lead-lag schedule are modified in such a way that the thrust coefficient equals the desired value and both rotor plane moment coefficients are zero.

For a helicopter rotor the pitch schedule is given by

$$\theta = \theta_0 + \theta_{1c} \cos\psi + \theta_{1s} \sin\psi$$

where ψ is the azimuth angle. Note that during the simulation of the Operational Loads Survey helicopter rotor in forward light the flap schedule has not been modified and no lead-lag schedule has been used.

The revolution-averaged thrust coefficient C_T and rotor plane moment coefficients C_{Mx} and C_{My} then depend on the collective pitch angle θ_0, the cosine-dependent pitch angle θ_{1c} and the sine-dependent pitch angle θ_{1s}.

The revolution-averaged thrust coefficient C_T mainly depends on the collective pitch angle θ_0, the revolution-averaged moment coefficient around the y-axis mainly depends on the cosine-dependent pitch angle θ_{1c} and the revolution-averaged moment coefficient around the x-axis mainly depends on the sine-dependent pitch angle θ_{1s}. Note that the x-axis points from the rotor to the tail-rotor, and that the y-axis points right looking from the tail-rotor to the rotor (pilot's view). The effect of adjusting the rotor collective and cyclic pitch on the thrust coefficient and rotor plane moment coefficients follows from taking the linear term of the Taylor-expansion of these equations, i.e.,

$$\begin{pmatrix} C_T \\ C_{My} \\ C_{Mx} \end{pmatrix}(\theta_0 + \Delta\theta_0, \theta_{1c} + \Delta\theta_{1c}, \theta_{1s} + \Delta\theta_{1s}) \approx$$
$$\begin{pmatrix} C_T \\ C_{My} \\ C_{Mx} \end{pmatrix}(\theta_0, \theta_{1c}, \theta_{1s})$$
$$+ \begin{bmatrix} \frac{\partial C_T}{\partial\theta_0} & \frac{\partial C_T}{\partial\theta_{1c}} & \frac{\partial C_T}{\partial\theta_{1s}} \\ \frac{\partial C_{My}}{\partial\theta_0} & \frac{\partial C_{My}}{\partial\theta_{1c}} & \frac{\partial C_{My}}{\partial\theta_{1s}} \\ \frac{\partial C_{Mx}}{\partial\theta_0} & \frac{\partial C_{Mx}}{\partial\theta_{1c}} & \frac{\partial C_{Mx}}{\partial\theta_{1s}} \end{bmatrix}(\theta_0, \theta_{1c}, \theta_{1s}) \begin{pmatrix} \Delta\theta_0 \\ \Delta\theta_{1c} \\ \Delta\theta_0 \end{pmatrix}$$

Here $\Delta\theta_0$, $\Delta\theta_{1c}$ and $\Delta\theta_{1s}$ indicate the small changes in the collective, cosine-dependent and the sine-dependent cyclic pitch, respectively. The coefficients in the matrix are the sensitivities of

the thrust coefficient and rotor plane moment coefficients to changes in the collective and cyclic pitch, with the diagonal terms being the dominant ones.
Since trim simulations are computationally intensive for Euler/Navier-Stokes-based methods, a lifting line vortex method (CAMRAD/JA[18]) has been used as a first estimate to calculate the sensitivities. The lifting line vortex method, however, only supplies the sensitivities of the thrust coefficient. To obtain the complete sensitivity matrix enabling the proper trimming of the helicopter rotor, three additional simulations with small variations (order one degree) of either the collective pitch, the cosine-dependent cyclic pitch or the sine-dependent cyclic pitch are performed with the Euler-based DG method. These simulations start from a periodic solution and are continued until the new solution also is periodic. For the simulation of the OLS helicopter rotor in forward flight, the simulations consisted of one revolution due to the small transient (only a quarter of a revolution). The second half of this revolution has been used to obtain the forces needed for the sensitivity calculation.

4 Grid adaptation

The general idea behind grid adaptation is that to minimize the numerical diffusion of the vorticity and the numerical dissipation in a vortex, the grid within the vortex should be as isotropic, as uniform and as refined as possible.
The grid adaptation algorithm consists of the following parts:

(i) the grid adaptation sensor. Basically, two types of sensors are available: (1) sensors that measure differences of flow quantities across element faces, and (2) sensors that measure the magnitude of a flow variable in an element. An example of the first sensor type is the standard shock sensor, which measures flow ‘gradients’ (actually differences) of the five conserved variables and the total pressure loss across element faces. An example of the second sensor type is the vortex sensor based on, for example, the vorticity magnitude. In addition to these sensors one can also use a grid quality sensor, i.e., a sensor that measures the jump in the mesh width in the direction normal to the element face, an anisotropy sensor, i.e., a sensor that measures the anisotropy (aspect ratios) of an element, and, a uniformity sensor, i.e., a sensor that measures the mesh width in each coordinate direction.

(ii) the grid adaptation type. The two basic types of grid adaptation are isotropic and anisotropic grid adaptation. If a sensor contains directional information (such as the shock sensor), anisotropic grid adaptation is used. The element is adapted in the direction associated with the gradient. If a sensor contains no directional information, isotropic refinement is used.

(iii) the grid adaptation control. The adaptation control determines for example the adaptation frequency and the percentage of elements that will be removed or refined.

For the helicopter rotor in hover simulations discussed in the next section the vortex sensor based on the vorticity magnitude ($|\omega|$) is used, combined with a uniformity sensor, resulting in uniform meshes of specified widths (typically 0.005 rotor diameters, i.e., 2.5 times the required width reported by Caradonna[9]) in the vortex. The grid adaptation sensor used in the forward flight simulation was a combination of the vortex sensor based on the vorticity magnitude with the anisotropy sensor or the uniformity sensor, resulting once more in uniform meshes of specified width (typically 0.005 rotor diameters) in the vortex.

With respect to the adaptation frequency for time-accurate, time-periodic simulations, such as the simulation of a helicopter rotor in forward flight, two options exist: (i) simply adapt the grid at each implicit time step or, (ii) integrate the grid adaptation sensor over a complete period (e.g., corresponding to a user-specified azimuthal travel) and adapt the mesh based on this integrated sensor after the completion of the period. Both strategies have advantages and disadvantages. The first strategy is more efficient in terms of number of elements, since elements are both created and removed at each implicit time step. Moreover, with the grid being adapted during the period, faster convergence to a periodic flow solution is achieved. However, since grid adaptation results in a dynamic load-balancing problem, for which currently no scalable algorithms are known, the parallel efficiency of the flow solver will deteriorate. The second strategy resembles the classical adaptation strategy used in steady state problems. This method retains the parallel efficiency of the flow solver, but since the same adapted grid is used for all time steps the number of elements is larger than in the first strategy. A compromise between the two grid adaptation strategies is the following. At each implicit, time step the mesh is only ‘refined’ based on the instantaneous grid adaptation sensor and adaptation type. However, no elements are removed as is done in the first strategy. This effectively integrates the sensor in time, and allows for faster convergence to the periodic flow solution. For the simulation of the helicopter rotor in forward flight presented in the next section this compromise has been used.

Both adaptation strategies have their disadvantages. Either the number of elements is needlessly high, or a dynamic load-balancing problem is introduced. A new algorithm that does not suffer from these problems is presented in van der Ven[31].

5 Rotorcraft simulations

5.1 Caradonna-Tung helicopter rotor in hover

The standard Caradonna-Tung experiment has been conducted at NASA Ames and consists of a helicopter rotor in hover employing two cantilever-mounted, manually adjustable blades[8]. At five radial stations, viz. r/R=0.50, 0.68, 0.80, 0.89 and 0.96, pressure transducers were located. The experiments were performed for collective settings of 0, 2, 5, 8 and 12 degrees, and angular velocities ranging from 650 to 2450 rpm.

The flow field around the Caradonna-Tung helicopter rotor using a collective pitch setting of 12 degrees and a tip Mach number of 0.61 has been simulated using the discontinuous Galerkin finite element method.

The mutli-block grid generated at NLR of one half of the computational domain consists of 55 blocks, with a total of 726,784 elements. Simulations have been performed on this so-called 'fine grid'. In addition simulations have been performed on a one time coarser grid consisting of 90,848 elements ('medium grid') with grid adaptation. After grid adaptation using the vortex sensor based on the vorticity in combination with the uniformity sensor, the 'medium grid' contains 135,280 elements. The grid in the vortex was adapted to a uniform mesh width equal to 0.1c.

In Fig. 1 the surface pressure distribution at the three radial stations are compared with the experimental data[8]. The agreement between the simulations and the experimental data is generally good. The pressure peak at the lower side of the rotor blade is resolved better on the 'fine grid'. The results coincide very well with the experimental data at the lower side.

Fig. 2 shows the sectional thrust for the 'medium grid' with adaptation, the 'fine grid' and the experiment[8]. Both simulations show higher-than-measured thrust levels. The sectional thrust obtained on the 'fine grid' is higher than the one obtained on the 'medium grid' with adaptation, except for a small region near the rotor tip.

Fig. 3 shows the vorticity contours at the 140 degrees azimuth location behind the blade for the 'medium grid' with grid adaptation and the 'fine grid'. From these results it can be seen that grid adaptation improves the vortex signature in terms of vorticity. Comparing these results with those presented by Raddatz[23] shows that the discontinuous Galerkin finite element method is able to carry vorticity over a longer distance and thus provides a clearer vortex signature.

It should, however, be noted that the 'medium grid' with grid adaptation consists of 135,280 elements with 20 degrees of freedom per element, resulting in a total of 2,705,600 degrees of freedom, which is almost twice as much as the 1,433,600 degrees of freedom reported by Raddatz[23].

The local behavior of the grid adaptation is presented in Fig. 4. Here, rotor blade 1, the periodic plane at z=0 and the plane at x=-3.6 are shown. Clearly visible are the places where the vortex

intersects these planes. At those positions one can see that the grid has been adapted to obtain a grid as isotropic and as uniform as possible in the vortex.

Fig. 5 shows iso-contours of the vorticity for the simulations on the 'fine grid'. From this figure it is clear that the discontinuous Galerkin finite element method is able to capture the tip vortex over a distance of at least one-and-a-half revolution, provided the multi-grid iterations are continued until all the residuals of the 20 non-linear algebraic equations per element are sufficiently converged. For the present simulations a convergence of three orders was deemed sufficient. Note that the distance of one-and-a-half revolution equals the required distance for accurate blade-vortex interaction predictions. The convergence tolerance for the accurate capture of trailing vortices is, however, significantly tighter than the equivalent convergence tolerance needed to capture transonic shock waves.

Finally, Fig. 6 gives a quantitative comparison between the predicted and the experimental measured vortex trajectory up to an azimuth angle of 540 degrees, i.e., one-and-a-half revolution behind the rotor blade. The agreement between the measured and the computed vertical position is good, except for the region close to the blade. The predicted radial contraction of the tip vortex shows reasonable agreement with the experimental data. The agreement between the simulation on the 'medium grid' with adaptation and the 'fine grid' is generally good.

The presented results, i.e. the surface pressure distributions, the sectional thrust and the vortex trajectories, are similar to the ones reported in Ahmad[1], where the grid dependency of the rotor wake was studied for the case having a collective pitch setting of 8 degrees and a tip Mach number of 0.439. Three different (background) grids having uniform mesh spacings (0.2c, 0.1c and 0.05c) were compared during this study.

5.2 Operational Loads Survey helicopter rotor simulations

The capabilities of the discontinuous Galerkin flow solver with respect to the simulation of a helicopter rotor in forward flight have been tested against the Operational Loads Survey helicopter rotor experiment[7]. The Operational Loads Survey helicopter rotor corresponds to a 1/7-scale model of the AH-1 helicopter rotor. The planform of the AH-1G/OLS rotor is rectangular and the blade section equals a modified BHT-540 section. The airfoil has been modified in order to accommodate full-scale pressure instrumentation during the experiment. The resulting thickness is 9.71% of the chord length. The diameter of the rotor is 1.916m and the chord length is 0.1039m. The blades have a root cutout at 18.2 % of the rotor radius. The rotor blades are twisted 10 degrees from the blade root to the blade tip. In rest the blade pitch angle at the 75% radial station is zero. All blade pitch angles are specified with respect to this station. The Operational Loads Survey helicopter rotor blades rotate about quarter-chord.

The Operational Loads Survey helicopter rotor experiment has been conducted in the German-Dutch wind tunnel (DNW) in order to gather rotor-blade pressures and far field radiated noise.

At five radial stations, viz. r/R=0.75, 0.80, 0.85, 0.91 and 0.975, pressure transducers were located at the three percent chordwise station on both the upper and the lower side of the blade. The ranges of the four governing non-dimensional parameters tested are

(1) the tip mach number M_{tip}: 0.55 …. 0.72,
(2) the advance ratio μ: 0.13 …. 0.35,
(3) the thrust coefficient C_T: 0.0047 …. 0.0080, and
(4) the tip-path plane angle α_{TPP}: -5 …. 7 degrees.

The flow field around the Operational Loads Survey helicopter rotor in forward flight has been simulated for the flow conditions of RUN 3020[7], i.e., a tip Mach number M_{tip} of 0.664, an advance ratio μ of 0.164, a thrust coefficient C_T of 0.0054 and a tip-path plane angle α_{TPP} of 2 degrees. This case corresponds to the following flight conditions: (i) a forward velocity of the rotor of 72 knots, i.e., 37 m/s, and (ii) a rate of descent of approximately 400 ft/min, i.e., 2 m/s. The simulation has been performed on a multi-block grid generated at NLR consisting of 72 blocks with an initial total of 244,224 elements.

The complete simulation consisted of several revolutions. A constant increment of the azimuth angle, i.e., 1.25 degrees, has been used. During the simulation the grid has been adapted twice. During the first adaptation (lasting half of a revolution) the vortex sensor based on the vorticity magnitude has been used in combination with the anisotropy sensor, resulting in a grid of 488,026 elements. During the subsequent second adaptation (lasting one full revolution) the vortex sensor based on the vorticity magnitude has been used in combination with the uniformity sensor. The grid in the vortex was adapted to a uniform mesh width equal to 0.005D. At each implicit time step the mesh has only been refined. Since no elements are removed, in this manner the vortex sensor is effectively integrated in time. After adaptation the grid contains 1,297,729 elements.

Several settings for the blade motion coefficients have been used during the simulation. Two combinations of blade motion coefficients and computational grids will be shown here. Firstly, on the grid consisting of 488,026 elements a simulation has been performed using the blade motion coefficients denoted as Schedule 1 in Tab. 1 (no lead/lag schedule has been used). Secondly, on the grid consisting of 1,297,729 elements a simulation using the blade motion coefficients denoted as Schedule 2 in Tab. 1 has been performed. To obtain the pitch angles for this case the previously described trimming procedure using the complete sensitivity matrix for the pitch angles has been applied.

Fig. 7 shows the differential pressure at the three percent chordwise station at r/R=0.975 for these two cases. It can be seen that the result obtained using Schedule 2 is significantly closer to the experiment than the result obtained using Schedule 1. Although the effects of trimming and grid adaptation intertwine during these simulations, the overall improvement has been obtained by the trimming.

The obtained revolution-averaged thrust coefficient and rotor plane moment coefficients are shown in Tab. 2. Although the revolution-averaged thrust coefficient for Schedule 2 is slightly higher than the experimental value of 0.0054, the revolution-averaged rotor plane moment coefficients are small compared with those of Schedule 1 and of Strawn[26]. In Fig. 8 the differential pressure at the three- percent chordwise station at r/R=0.975 for Schedule 2, Strawn[26] and the experiment are shown. Note that Strawn[26] performed his simulations on a grid consisting of 1.8 million grid points and that during his simulation a constant increment of the azimuth angle of 0.25 degrees was used.

In Fig. 9 the differential pressure at the three percent chordwise station for Schedule 2 is compared with the experimental data obtained at the five radial stations, where pressure transducers were located. The agreement between the differential pressures obtained during the simulation and the experiment is generally good. As can be seen in this figure the overall agreement between the results obtained during the simulation and the experimental results improves with increasing radial position r/R. Several blade-vortex interaction events can be observed. Comparing this figure with previously reported Euler and Navier-Stokes simulations for the Operational Loads Survey helicopter rotor in forward flight[21,26] (see also Fig. 8), one can see that with the present method a considerable improvement has been obtained.

In Fig. 10, the sectional lift, the differential pressure at the three percent chordwise station and the derivatives of the sectional lift and the differential pressure at that station with respect to the azimuth angle are shown. On both the advancing side and the retreating side the present simulation finds two interactions. Starting from $\psi=0°$ and looking in counter clockwise direction, the rotor blade first interacts parallel (PI) with a vortex originating from the blade itself, next it interacts perpendicular (PPI) with the vortex originating from the other blade, then there is once more an interaction with the vortex originating from the other blade which initially is perpendicular but develops into an oblique interaction (OI), and finally the blade interacts with a vortex originating from itself. This final interaction starts as a parallel interaction (PI) but develops into an oblique interaction (OI). In this figure the effect of the root vortices can be clearly seen by the interactions around the zero azimuth angle. It is obvious that the presence of these vortices, which are not present in the experiment due to a different geometry in the hub region, influences the solution.

6 Summary

In this report the DG finite element algorithm based on a boundary conforming ALE formulation in conjunction with unstructured grid refinement of hexahedral grids has been used for the simulation of rotor wake vortices.

The following simulations have demonstrated the simulation capabilities of this flow solver:

- the Caradonna-Tung helicopter rotor in hover, showing that this method is able to capture the tip vortex over a distance of at least one-and-a-half revolution, both on a 726,784-element grid and a 135,280-element grid with local unstructured grid refinement, and
- the Operational Loads Survey helicopter rotor in forward flight, showing the methods ability to perform time-accurate helicopter simulations on a single boundary conforming grid.

All simulations showed that local grid adaptation, when applied, improves the vortex signature in terms of vorticity and/or helicity. Comparison with the experimental data is generally good. For the forward flight simulation, the rotor trimming procedure as developed at NLR has been used.

It was shown that, using this procedure, one obtains considerably improved results compared with previously reported Euler and Navier-Stokes simulations. These improvements are due to the fact that all sensitivity coefficients with respect to the pitching parameters are used, and that the sensitivity matrix is calculated using the Euler flow solver itself, instead of using a lifting line vortex method, such as CAMRAD/JA.

The presented discontinuous Galerkin method has the following features that make it well suited for the simulation of rotor wake flows:

(a) the second-order accurate DG method carries the spatial flow field gradients as explicit, dependent variables implying that the vorticity is carried as a dependent flow variable; vorticity components are implicitly related to the three spatial gradients of the state vector (15 variables per element),

(b) the algorithm allows degenerate, high-aspect ratio elements near leading and trailing edges for efficiency,

(c) the algorithm has an extremely compact stencil, and as a result possesses an inherent ability to handle adaptive strategies since the refining and de-refining of the elements (grid) is done without any need to consider special continuity requirements typical of conventional CFD methods[29], and

(d) the algorithm has an excellent parallelization potential because the communication between neighboring elements is strictly limited to the flow data exchange at common faces, and will therefore be well suited for parallel computing platforms.

Furthermore, it should be noted that an extension of the DG algorithm from the Euler equations to the Navier-Stokes equations is feasible without compromising items (a) through (d) above,

e.g., see Atkins[2] for an analysis in two dimensions. With respect to vortex flow simulations the main difference between a simulation using the Euler equations and a simulation using the Navier-Stokes equations is that for the former grid adaptation results in an unlimited increase of the vortex resolution.

7 Conclusions

The main issue explored in the present report is the ability of the discontinuous Galerkin finite element approach to capture the tip vortex of a rotor over large distances (with and without grid adaptation). The conclusion is that the present DG algorithm can capture the tip vortex of a rotor in hover or forward flight over large distances, provided the multi-grid iterations are continued until all the residuals of the 20 non-linear, algebraic equations per element are sufficiently converged. It is found that the convergence tolerance required for the accurate capture of trailing vortices is significantly tighter than the equivalent convergence tolerance needed to capture transonic shock waves; i.e., transonic shock waves are easy to capture relative to the far field signature of trailing vortices.

Comparison of results of the present DG method (with and without adaptation) with the results of more conventional algorithms[21-23,26] shows that the present DG approach yields the same or better agreement between CFD and experimental data in terms of blade surface pressures, differential pressures and vortex trajectories.

For accurate prediction of the flow around a rotor in forward flight, it was concluded that trimming of the rotor is of utmost importance. The trimming procedure developed at NLR resulted in substantially improved differential pressure distributions when compared with those presented in literature[21,22,26]. Pahlke[22] remarks the following: ‘It was shown that the viscous effects are important for the prediction of the global forces but the effect of trim is even more important’. This remark stresses the above-mentioned importance of proper trimming.

Acknowledgements

The authors would like to acknowledge the support of the Royal Netherlands Air Force (RNLAF, contract number N98/19), The Boeing company Mesa and NLR; we would also like to thank J. van Muijden, S.P. Spekreijse and H.A. Sytsma of NLR for making the grids, and J.J.W. van der Vegt of the University of Twente, Enschede, The Netherlands for his contributions to the discontinuous Galerkin finite element flow solver algorithm.

References

[1] Ahmad, J.U, and Strawn, R.C., "Hovering Rotor and Wake Calculations with an Overset-Grid Navier-Stokes Solver," *Paper presented at American Helicopter Society 55th Annual Forum*, Montreal, Canada, 1999.

[2] Atkins, H.L., and Shu, C.W., "Analysis of the Discontinuous Galerkin Method to the Diffusion Operator," AIAA Paper 99-3306, 1999.

[3] Boelens, O.J., van der Ven, H., Oskam, B. and Hassan, A. A., "Accurate and Efficient Vortex-Capturing for Rotor Blade-Vortex Interaction,'' AIAA Paper 2000-0112, 2000.

[4] Boelens, O.J., van der Ven, H., Oskam, B. and Hassan, A.A., "Accurate and Efficient Vortex-Capturing for a Helicopter Rotor in Hover," *Paper presented at 26th European Rotorcraft Forum*, The Hague, The Netherlands, 2000.

[5] Boniface, J.-C. and Pahlke, K., "Calculations of Multibladed Rotors in Forward Flight using 3D Euler Methods of DLR and ONERA," *Paper presented at 22nd European Rotorcraft Forum*, Brighton, United Kingdom,1996.

[6] Bottasso, C.L. and Shephard, M.S., "Parallel Adaptive Finite Element Euler Flow Solver for Rotary Wing Aerodynamics,'" *AIAA Journal*, Vol. 35, 1997, pp. 937-944.

[7] Boxwell, D.A., Schmitz, F.H., Splettstoesser, W.R. and Schultz, K.J., "Helicopter Model Rotor-Blade Vortex Interaction Impulsive Noise: Scalability and Parametric Variations," *Journal of American Helicopter Society*, Vol. 32, 1987, pp. 3-12.

[8] Caradonna, F.X. and Tung, C., "Experimental and Analytical Studies of a Model Helicopter Rotor in Hover," NASA Technical Memorandum 81232, 1981.

[9] Caradonna, F.X., "Development and Challenges in Rotorcraft Aerodynamics," AIAA Paper 2000-0109, 2000.

[10] Cockburn, B., "Discontinuous Galerkin Methods for Convection-Dominated Problems," *High-order methods for computational physics*, edited by T. Barth and H. Deconinck, Lecture Notes in Computational Science and Engineering, Vol. 9, Springer Verlag, 1999.

[11] Cockburn, B., Karniadakis, G. and Shu, C.-W., "An Overview of the Development of Discontinuous Galerkin Methods," Lecture Notes in Computational Science and Engineering, Vol. 11, Springer Verlag, 1999.

[12] Devine, K.D. and Flaherty, J.E., "Parallel adaptive *hp*-refinement techniques for conservation laws," *Applied Numerical Mathematics: Transactions of IMACS*, Vol. 20, No. 4, 1996, 367-386.

[13] Dindar, M., "An Adaptive Finite Element Procedure for Rotorcraft Aerodynamics and Aeroelasticity," Rensselaer Polytechnic Institute, Troy, New York, 1998.

[14] Dindar, M., Shephard, M.S., Flaherty, J.E. and Jansen, K., "Adaptive CFD Analysis for Rotorcraft Aerodynamics," *Comput. Methods Appl. Mech. Engrg.*, Vol. 189, 2000.

[15] Duque, E.P.N. and Srinivasan, G.R., "Numerical Simulations of a Hovering Rotor using Embedded Grids," *Paper presented at American Helicopter Society 48th Annual Forum*, Washington DC, USA, 1992.

[16] Duque, E.P.N., Strawn, R.C., Ahmad, J. and Biswas, R., "An Overset Grid Navier-Stokes Kirchhoff-Surface Method for Rotorcraft Aeroacoustic Predictions," AIAA Paper 96-0152, 1996.

[17] Hariharan, N. and Sankar, L.N., "A Review of Computational Techniques for Rotor Wake Modeling," AIAA Paper 2000-0114, 2000.

[18] Hassan, A.A., Charles, B.D, Tadghighi, H. and Burley, C., "A Consistent Approach for Modeling the Aerodynamics of Self-Generated Rotor Blade-Vortex Interactions," *Journal of the American Helicopter Society*, April 1996, pp. 74-84.

[19] Kondo, N., Ochi, A., Nakamura, H., Aoyama, T., Saito, S. and Yamakawa, E., "Validation of Rotor Aerodynamic and Acoustic Prediction Methods using ATIC 2nd Model Rotor," *Paper presented at 26th European Rotorcraft Forum*, The Hague, The Netherlands, 2000.

[20] Ochi, A., Aoyama, T., Saito, S., Shima, E. and Yamkawa, E., "BVI noise Predictions by Moving Overlapped Grid Method," *Paper presented at 55th American Helicopter Society Annual Forum*, Montreal, Canada, 1999.

[21] Pahlke, K., "Berechnung von Strömungsfeldern um Hubschrauberrotoren im Vorwärtsflug durch die Lösung der Euler-Gleichungen," Forschungsbericht 1999-22, Deutsches Zentrum für Luft- und Raumfahrt e. V., 1999

[22] Pahlke, K. and Chelli, E., "Calculation of Multiblade Rotors in Forward Flight Using a 3D Navier-Stokes Method," *Paper presented at 26th European Rotorcraft Forum*, The Hague, The Netherlands, 2000

[23] Raddatz, J. and Pahlke, K., "Calculations of Multibladed Rotors in Hover using 3D Euler Methods of DLR and ONERA," *Paper presented at 21st European Rotorcraft Forum*, Saint Petersburg, Russia, 1995.

[24] Srinivasan, G.R., Baeder, J.D., Obayashi, S. and McCroskey, W.J., "Flowfield of a Lifting Rotor in Hover: A Navier-Stokes Simulation," *AIAA Journal*, Vol. 30, 1992, pp. 2371-2378.

[25] Strawn, R.C., Biswas, R. and Lyrintzis, A.S., "Helicopter Noise Predictions using Kirchhoff Methods," *Journal of Computational Acoustics*, Vol. 4, 1996, pp. 321-339.

[26] Strawn, R.C., Ahmad, J. and Duque, E.P.N., "Rotorcraft Aeroacoustics Computations with Overset-Grid CFD Methods," *Paper presented at the 54th American Helicopter Society Annual Forum*, Washington, DC, USA, 1998.

[27] Strawn, R.C. and Ahmad, J., "Computational Modeling of Hovering Rotors and Wakes," AIAA Paper 2000-0110, 2000.

[28] van der Vegt, J.J.W. and van der Ven, H., "Discontinuous Galerkin Finite Element Method with Anisotropic Local Grid Refinement for Inviscid Compressible Flow.," *J. Comput. Phys*., Vol. 140, 1998, pp. 1-32.

[29] van der Vegt, J.J.W., and van der Ven, H., "Space-Time Discontinuous Galerkin Finite Element Method With Dynamic Grid Motion For Inviscid Compressible Flow. Part I. General Formulation," submitted to J. Comput. Phys., 2002.

[30] van der Ven, H. and van der Vegt, J.J.W., "Accuracy, Resolution, and Computational Complexity of a Discontinuous Galerkin Finite Element Method," Lecture Notes in Computational Science and Engineering, Vol. 11, Springer Verlag, 1999.

[31] van der Ven, H., Boelens, O.J. and Oskam, B., "Multitime multigrid convergence acceleration for periodic problems with future applications to rotor simulations," *International Parallel CFD 2001 Conference*, Eds. P. Wilders et al., North-Holland Elsevier, 2002.

[32] Webster, B.E., Shephard, M.S., Rusak, Z. and Flahery, J.E., "Automated Adaptive Time-Discontinuous Finite Element Method for Unsteady Compressible Airfoil Aerodynamics," *AIAA Journal*, Vol. 32, 1994, pp. 748-757.

[33] Wissink, A.M., Lyrintzis, A.S., Strawn, R.C., Oliker, L. and Biswas, R., "Efficient Helicopter Aerodynamic and Aeroacoustic Predictions on Parallel Computers," AIAA Paper 96-0153, 1996.

[34] Yang, Z., Sankar, L., Smith, M. and Bauchau, O., "Recent improvements to a hybrid method for rotors in forward flight," AIAA Paper 2000-0260, 2000.

	θ_0[°]	θ_{1c}[°]	θ_{1s}[°]	β_0[°]	β_{1c}[°]	β_{1s}[°]
Schedule 1	6.53	0.90	-1.39	2.40	-1.00	0.00
Schedule 2	6.62	2.81	-2.19	2.40	-1.00	0.00
Strawn[26]	6.14	0.90	-1.39	0.50	-1.00	0.00

Table 1: Pitch and flap angles used in the simulation of the Operational Loads Survey helicopter rotor in forward flight.

	C_T ($\times 10^3$)	C_{Mx} ($\times 10^3$)	C_{My} ($\times 10^3$)
Experiment	5.40	0.00	0.00
Schedule 1	5.440	0.161	0.519
Schedule 2	5.553	0.037	-0.112
Strawn[26]	5.43	0.11	0.41

Table 2: Force and moment data from the simulation of the Operational Loads Survey helicopter rotor in forward flight. Experimental data is taken from Strawn [26].

Code name	Main technique	Flow conservation	Adaptivity	Scalability	Accuracy
ASTRA-OG[19,20]	Chimera/Overset	ʒ	-	-	+
FLOWER[21]	Chimera/Overset	ʒ	-	-	ʒ
FLOWER[22]	Chimera/Overset	ʒ	-	-	ʒ
OVERFLOW[26]	Chimera/Overset	ʒ	ʒ	-	ʒ
DG flow solver	Boundary conforming	+	+	ʒ	+

Code name	Rotor type	Number of blades	Number of grid points ($\times 10^6$)	Computing time for one revolution	Flop count ($\times 10^{12}$)
ASTRA-OG	ATIC AT2	5	17.0	20 hours on NWT/30	1100
FLOWER	OLS	2	1.4	107 hours on Cray J916/1	58
FLOWER	ONERA 7AD	4	2.0	23.5 hours on NEC SX-5/1	135
OVERFLOW	OLS	2	1.8	15 hours on Cray C-90/1	16
DG flow solver	OLS	2	1.2	20 hours on NEC SX-5/8	1150

Table 3: Qualitative comparison and computing times of existing rotor codes for forward flight simulations. NWT: Numerical Wind Tunnel (parallel vector machine with 1.7 Gflop/s peak per processor), Cray J916: parallel vector machine with 0.5 Gflop/s peak per processor, Cray C-90 parallel vector machine with 1 Gflop/s peak per processor, NEC SX-5 parallel vector machine

with 8 Gflop/s peak per processor. The flop counts are estimated from the computing times and an assumed sustained performance of 30 % on vector processors.(- = unsatisfactory, ƺ = fair, + = good). Data is taken from Kondo[19], Ochi[20], Pahlke[21,22] and Strawn[26].

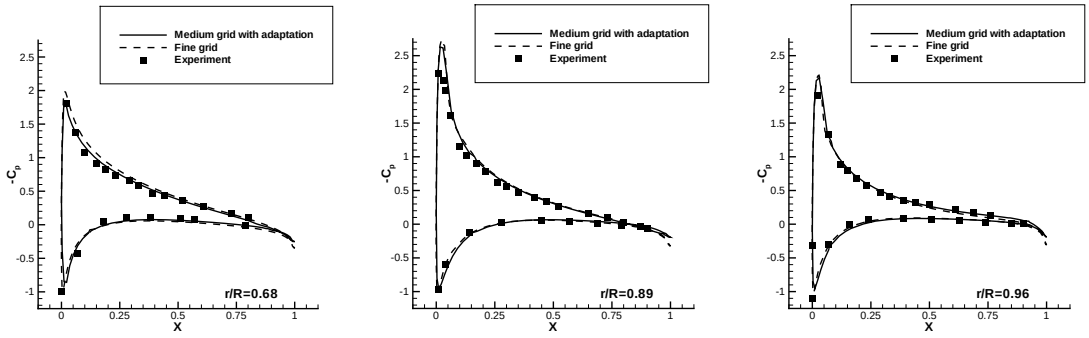

(a) (b) (c)

Figure 1: Surface pressure ($-C_p$) distribution at the radial stations r/R=0.68 (a), 0.89 (b) and 0.96 (c) for the Caradonna-Tung helicopter rotor in hover (collective pitch angle: 12 degrees, tip Mach umber: 0.61, Reynolds number: $2.7 \cdot 10^6$). Experimental data is taken from Caradonna[8].

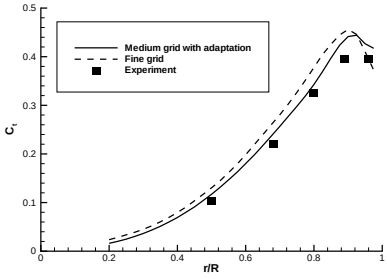

Figure 2: Sectional thrust for the Caradonna-Tung helicopter rotor in hover for the 'medium grid' with adaptation (135,280 elements), the 'fine grid' (726,784 elements) and the experiment8 (collective pitch angle: 12 degrees, tip Mach number: 0.61).

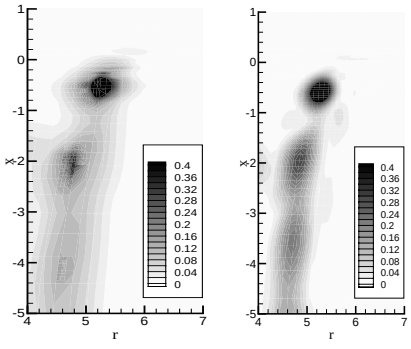

(a) (b)

Figure 3: Vorticity contours at the 140 degree azimuth location behind the blade for the Caradonna-Tung helicopter rotor in hover on the 'medium grid' with adaptation (a) (135,280 elements) and on the 'fine grid' (b) (726,784 elements) (collective pitch angle: 12 degrees, tip Mach number: 0.61).

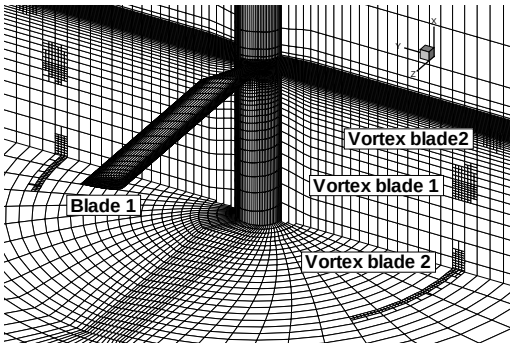

Figure 4: The adapted Caradonna-Tung grid (135,280 elements). Shown are the periodic plane at z=0 and the plane at x=-3.6.

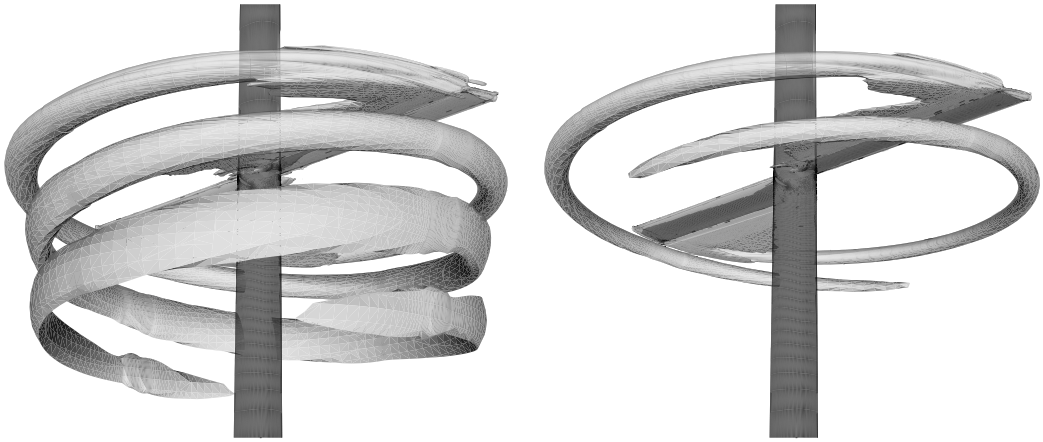

Figure 5: Iso-contour of the vorticity for the Caradonna-Tung helicopter rotor in hover on the 'fine grid' (726,784 elements) (collective pitch: 12°, Mtip=0.61).

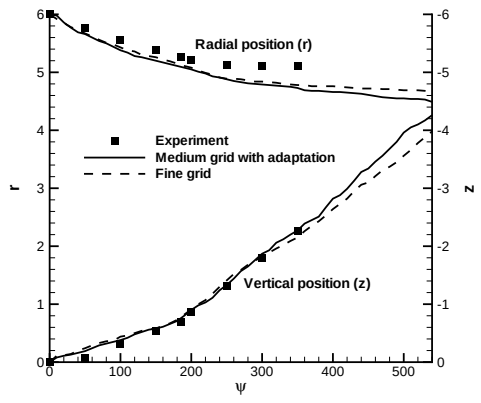

Figure 6: Predicted and experimental vortex trajectory of the Caradonna-Tung rotor in hover on the 'medium grid' with adaptation (135,280 elements and on the 'fine grid' (726,784 elements) (collective pitch angle: 12 degrees, tip Mach number: 0.61). The upper lines indicate the radial position of the vortex and the lower lines indicate the vertical position of the vortex.

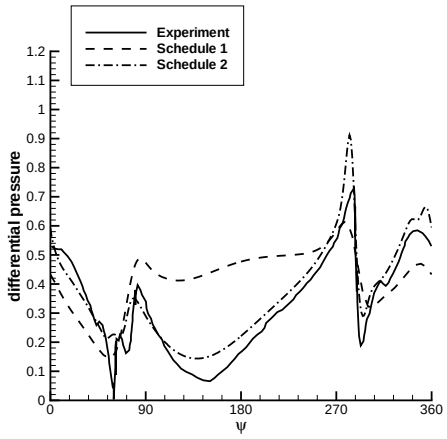

Figure 7: Differential pressure -$\Delta C_p M^2$ at the three percent chordwise station at r/R=0.975 for Schedule 1, Schedule 2 and the experiment. For Schedules 1 and 2 see Tab. 1.

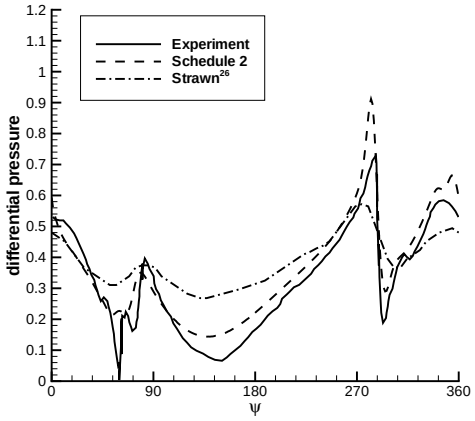

Figure 8: Differential pressure -ΔCpM2 at the three percent chordwise station at r/R=0.975 for the Schedule 2, Strawn26 and the experiment.

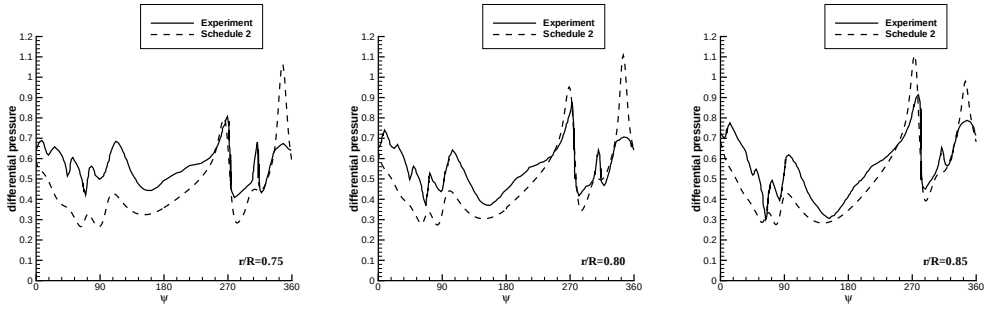

(a) (b) (c)

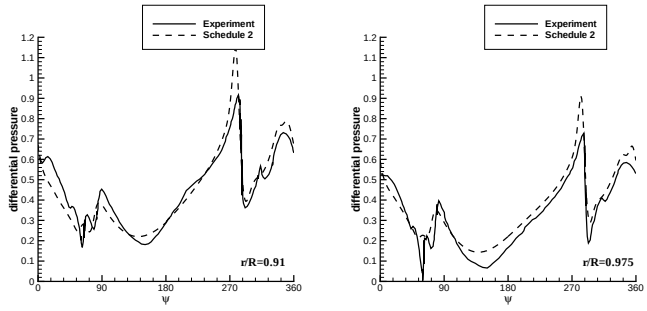

(d) (e)

Figure 9: Differential pressure -ΔCpM2 at the three percent chordwise station at the radial stations r/R=0.75 (a), 0.80 (b), 0.85 (c), 0.91 (d) and 0.975 (e) for the Operational Loads Survey helicopter rotor in forward flight.

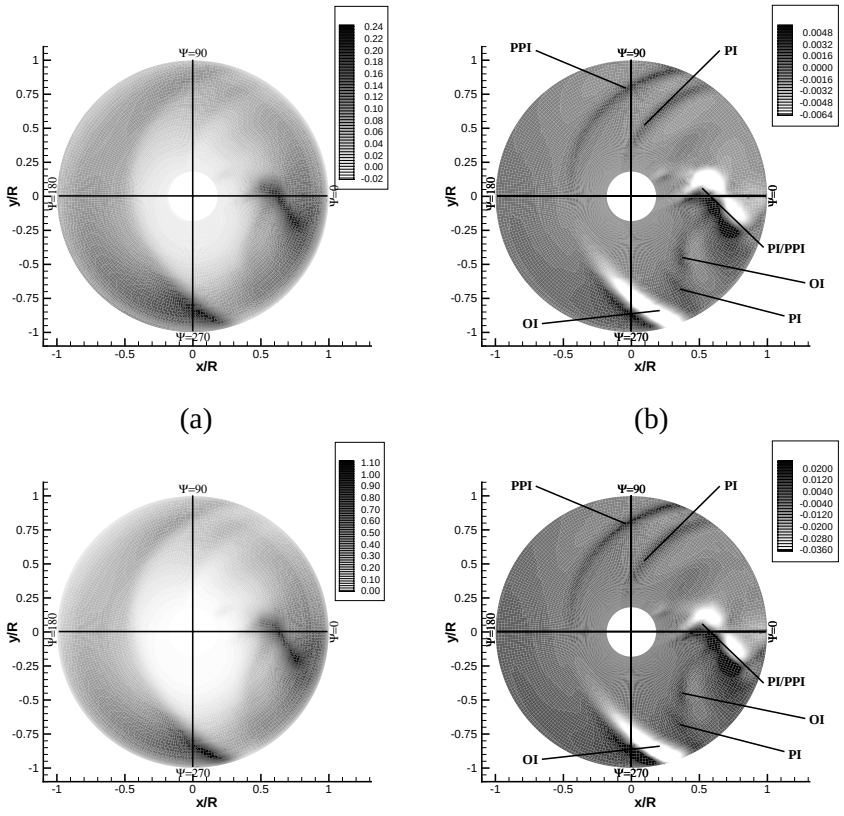

(a) (b)

(c) (d)

Figure 10: The sectional lift (a), the derivative of the sectional lift with respect to ψ (b), the differential pressure -ΔCpM2 at the three percent chordwise station (c) and the derivative of the differential pressure -ΔCpM2 at the three percent chordwise station with respect to ψ(d) for Schedule 2; PI: parallel interaction, PPI: perpendicular interaction, OI: oblique interaction.